Metals and Materials International (2021) 27:384–391
https://doi.org/10.1007/s12540-019-00430-z

Effects of β Air Cooling and Subsequent Cold Rolling on Microstructure and Hardness of Zr702 Sheet

Haotian Guan[1] · Lingguo Zeng[2] · Zhijun Li[2] · Linjiang Chai[1] · Yufan Zhu[1] · Yueyuan Wang[1] · Qin Huang[1] · Ke Chen[1] · Liang-yu Chen[3] · Ning Guo[4]

Received: 13 May 2019 / Accepted: 11 August 2019 / Published online: 20 August 2019

Abstract
In this work, a Zr702 sheet was subjected to β air cooling and then rolled to 15% reduction at room temperature, with their detailed microstructural characteristics characterized by electron channeling contrast imaging and electron backscatter diffraction techniques. Results show that after the β air cooling, the prior equiaxed grains in the as-received material are completely transformed into Widmanstätten structures featured by coarse plates with typical phase transformation misorientations between them. The subsequent 15% rolling allows both slip and twinning (especially the {10–12} type) to be activated readily, leading to significant grain refinement and the appearance of misorientation angle peaks around 3°–5° and 85°. Analyses on kernel average misorientations reveal that there exist very low residual strains in the β-air-cooled specimen while they are markedly increased after the 15% rolling and preferably distributed near low-angle and twin boundaries. Hardness measurements show that the specimen hardness is evidently decreased from ~ 199 to ~ 170 HV after the β air cooling, which can be attributed to grain coarsening and the scattered orientations associated with the slow β → α transformation. For the 15%-rolled specimen, however, effective grain refinement by twinning and denser low-angle boundaries jointly lead to ~ 35% hardness increment to ~ 228 HV.

Keywords Zr sheet · Cold rolling · Hardness · Twinning · Electron backscatter diffraction

1 Introduction

Zr and its alloys have long been used as reactor fuel cladding materials thanks to their excellent nuclear properties (low thermal neutron cross-section) and good comprehensive mechanical properties [1–3]. At room temperature, most Zr alloys are mainly composed of hexagonal close-packed (hcp) α phases (α-Zr). Since a limited number of slip systems can be offered by the hcp structure, preferred orientations (textures) are often developed in processed Zr alloys and can significantly affect their final performance [4, 5]. For Zr alloys with a starting microstructure of equiaxed grains, much knowledge has to-date been documented on their microstructural and textural evolutions during typical rolling processings [6–11]. Note that during actual fabrications of Zr alloy products, β cooling treatments are frequently employed before subsequent rolling and annealing to reach optimized microstructural characteristics (especially second phase particles) and properties [12–14]. After the β cooling, the prior grain morphologies and crystallographic orientations will be significantly altered simultaneously. As a result, their deformation behaviors could be largely different from those of the equiaxed grains [15]. Hence, dedicated studies on microstructural characteristics of β-cooled Zr alloys during rolling should be able to provide important implications for optimized processings. However, in this regard, few results can be found in public literature and this motivates the present work.

✉ Linjiang Chai
chailinjiang@cqut.edu.cn

✉ Ning Guo
guoning_1000@163.com

[1] College of Materials Science and Engineering, Chongqing University of Technology, Chongqing 400054, China

[2] Chongqing Yufeng Wire and Cable Co., Ltd, Chongqing 402260, China

[3] School of Science, Jiangsu University of Science and Technology, Zhenjiang 212003, Jiangsu, China

[4] Faculty of Materials and Energy, Southwest University, Chongqing 400715, China

In this work, commercial Zr702 sheets were subjected to β air cooling and subsequent rolling (15% reduction) at room temperature. Electron channeling contrast (ECC) imaging and electron backscatter diffraction (EBSD) techniques were jointly employed to perform detailed microstructural characterizations for them. Hardnesses of the different specimens were also examined and correlated with the revealed microstructural features.

2 Experimental

The as-received materials were Zr702 sheets after 60% rolling at room temperature and recrystallization annealing at 600 °C for 1 h, with the initial thickness of 2 mm. Their chemical composition is listed in Table 1. The as-received sheets were heated at 1000 °C (complete β phase region) for 10 min in vacuum and then cooled to room temperature in air with an estimated cooling rate of ~ 5 °C/s. Subsequently, the β-air-cooled sheets were rolled at room temperature by 5% per pass to a thickness reduction of 15%, with the rolling plane and direction identical with those previously used for the as-received sheet. Rectangular specimens with dimensions of 12 and 10 mm along rolling and transverse directions (RD and TD) were cut from both the β-air-cooled and the 15%-rolled sheets.

A field emission gun scanning electron microscope (Zeiss Sigma HD) equipped with an back-scattered electron detector and an EBSD system was utilized to perform microstructural characterization for these specimens. The back-scattered electron detector allowed ECC images to be taken for direct microstructural observation [16, 17]. The EBSD system consisted of an Oxford Instruments NordlysMax^2 detector, with Aztec 2.4 software for orientation information acquisition and Channel 5 software for data post-processing, respectively. During the EBSD data acquisition, a scanning area of 180 μm and 140 μm along RD and ND (normal direction) was examined for each specimen at step sizes of 0.4–1 μm. Hardness measurements were performed for all specimens using a Vickers indentation machine (Everone MH-5L) at a load of 490 mN. At least twelve measurements were made for each specimen to calculate average values. Prior to microstructural examinations, RD-ND planes of all specimens were mechanically ground by SiC abrasive paper and then electro-polished in a mixed solution of 10% perchloric acid, 20% butyl cellosolve and 70% methanol at 20 V and − 30 °C for 0.5–1 min.

3 Results and Discussion

3.1 Microstructural Analyses

Figure 1 presents ECC images of the as-received, β-air-cooled and 15%-rolled specimens. As revealed in Fig. 1a, microstructures of the as-received material are comprised of well-equiaxed grains with relatively uniform sizes, suggesting sufficient recrystallization [18]. By use of the linear intercept method, their average grain size is measured to be ~ 8.5 μm. There are also a number of randomly distributed black dots in Fig. 1a and they should be second phase particles (SPPs). Figure 1b reveals that after the β-air-cooling treatment, all the prior equiaxed grains seem to be replaced by coarse plate structures, with their sizes (especially lengths) generally larger than those of the as-received material. Also, some fine SPPs are found to be distributed along plate boundaries, suggesting the occurrence of diffusional phase transformation. Such microstructural features in Zr alloys correspond to Widmanstätten structures [19]. From Fig. 1c, one can see that after the 15% rolling, contrasts of the plate structures become heterogeneous with the appearance of many twin-like lamellae. This suggests that plastic deformation readily occurs in the interior of the Zr702 sheet. As further revealed in Fig. 1d, such twin-like lamellae have distinct contrasts (orientations) from the matrix. Note that although the transformation microstructures after β → α cooling in Zr alloys may vary a lot at differnent cooling rates, the plate (or lammellar) structure (with varied plate widths) is usually found to be one common feature [20]. Thus, the present study on rolling microstructures of the β-air-cooled specimens should be able to provide definite implications for Zr alloys with other β-cooling treatments.

EBSD band contrast (BC) and inverse pole figure (IPF) maps of various specimens are displayed in Fig. 2. Figure 2a shows that the starting microstructure of the as-received material is composed of equiaxed grains, consistent with the ECC observation (Fig. 1a). Figure 2b further reveals that most of the equiaxed grains are colored near red and separated by high angle boundaries (HABs, θ > 15°). According to the color code in Fig. 2b, these red grains have their c-axes aligned close to the ND, suggesting remarkable orientation preference (crystallographic texture). From Fig. 2c, one can clearly see that the microstructure of the β-air-cooled specimen is comprised of plate structures. For adjacent parallel plates, Fig. 2d reveals that they tend to have the same orientation (color), leading to formation of some greatly coarsened grains. Grain sizes in Fig. 2d are measured by the linear intercept method to be

Table 1 Chemical composition of the Zr702 sheet (in wt%)

Hf	O	Fe	Cr	N	H	Zr
1.15	0.15	0.07	< 0.01	< 0.01	< 0.01	Bal

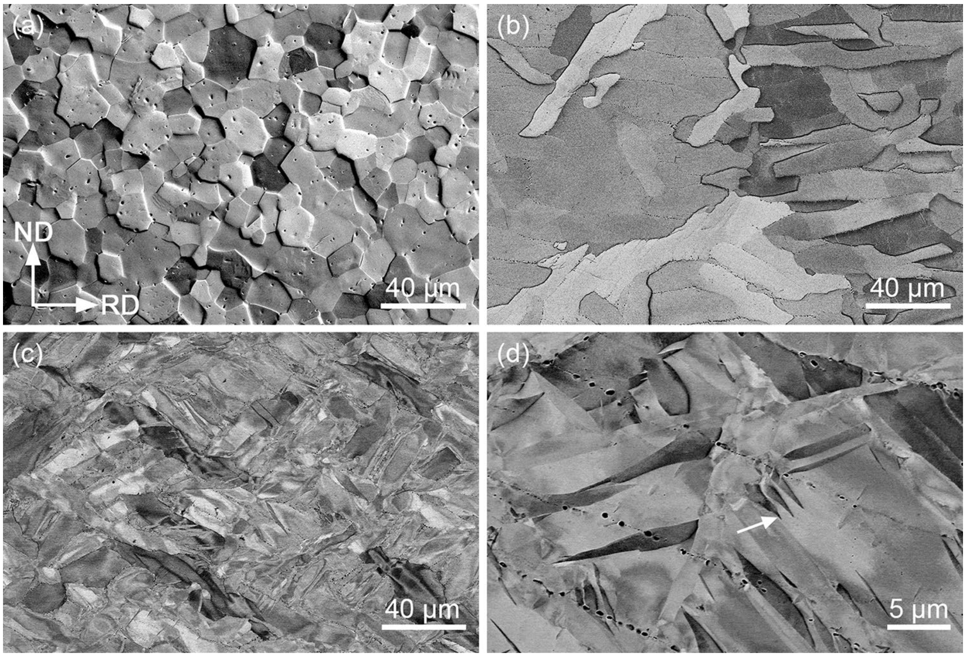

Fig. 1 ECC images of **a** the as-received, **b** the β-air-cooled and **c** the 15%-rolled specimens; **d** magnified observation of the 15%-rolled specimen with the white arrow indicating twin-like lamellae

14.5 μm on average. In contrast with the orientation preference in the as-received specimen, grain orientations in the β-air-cooled specimen is found to be largely scattered (Fig. 2d). This can be confirmed by the global texture measured by X-ray diffraction (already documented elsewhere [21]). Also from Fig. 2d, the plate colors are noted to be generally uniform and there exist few low angle boundaries (LABs, $2^\circ < \theta < 15^\circ$), indicating suppressed dislocation activities during the β air cooling. As for the 15%-rolled specimen, Fig. 2e shows that length directions of most plates are tilted towards the RD with many twin-like lamellae appearing, consistent with the case revealed in Fig. 1c and d. From Fig. 2f, orientations of the twin-like lamellae are confirmed to be largely different from the plate matrix. Meanwhile, inside most plates, highly heterogeneous colors with dense LABs can be observed, suggesting the occurrence of active dislocation slip during the rolling. Also from Fig. 2f, grain sizes of the 15%-rolled specimen are measured to be 5.7 μm on average, with an average aspect ratio of 5.0.

Figure 3 presents a dedicated analysis for some twin-like lamellae, corresponding to the boxed region in Fig. 2f. A comparison between Fig. 3a and b reveals that all the twin-like lamellae have a misorientation relationship of 85° ± 2°/<11–20> with the matrix, suggesting them to be {10–12} <10–11> tensile twins [5]. Previous studies [9, 22] demonstrated that rolling at room temperature would essentially not induce active twinning in typically textured Zr alloy sheets with equiaxed grains. Deformation twinning may play an important role in accommodating plastic strains when grain orientations are unfavorable for initiating slip. More specifically, {10–12} twinning occurs in an α-Zr grain only if its c-axis is subjected to a tensile stress, or a compressive stress is applied along its a-axis during deformation. One can see from Fig. 3c that there are only small angles (10°–15°) between the c-axis of the parent grain and the RD, suggesting the direction of tensile stress during rolling to be close to the c-axis. This will facilitate the initiation of tensile twinning (like {10–12} type), consistent with our observation. As further revealed in Fig. 3d, the c-axis of the parent grain is rotated by ~ 85° from near the RD to between the ND and the TD, as indicated by arrows in Fig. 3d.

Misorientation angle and rotation axis distribution histograms of all the three specimens are presented in Fig. 4. From Fig. 4a, the misorientation angle distribution (MAD) of the as-received specimen is found to be relatively uniform and random. Also, it indicates most boundaries belong to HABs while fractions of LABs are low, consistent with those revealed in Fig. 2b. In fact, compared to LABs, HABs are usually known to have higher mobility and their rapid migration is able to annex LABs during recrystallization [23]. In this work, the MAD features of the as-received specimen agree well with those of most recrystallized Zr alloy sheets [24]. After the β-air cooling, the MAD features are found to be markedly changed (Fig. 4b). There exist two peaks around 60° and 90° with their intensities significantly higher than others. It is known that the β → α transformation of Zr alloys usually follows the Burgers orientation relationship (OR), namely $\{0001\}_\alpha // \{110\}_\beta$ and $<11\text{–}20>_\alpha // <111>_\beta$ [25]. According to the Burgers OR, twelve α orientations (variants) can be produced from one β orientation and there are five possible misorientations (10.5°/<0001>, 60°/<11–20>, 60.8°/<1 1.38–2.38 0.36>, 63.3°/<5 5–10 3> and 90°/<1

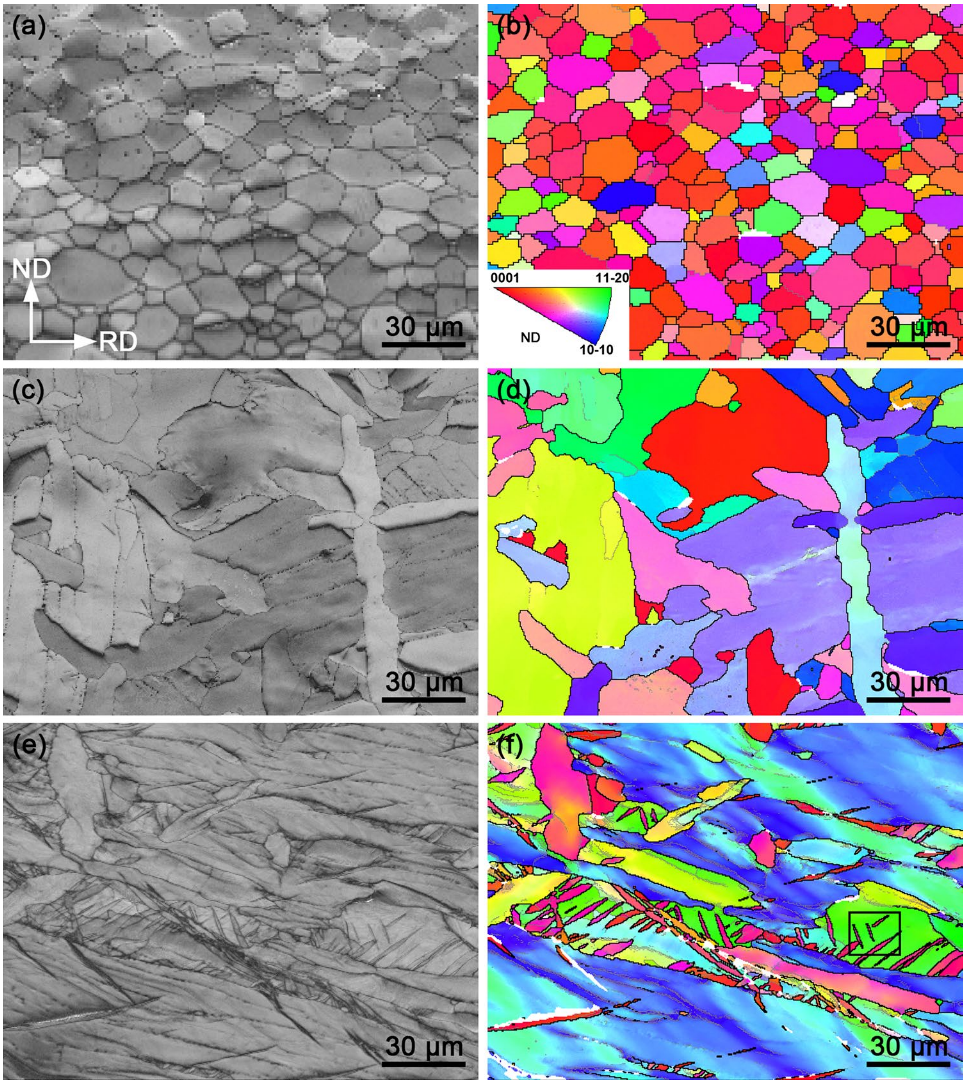

Fig. 2 EBSD BC maps of **a** the as-received, **c** the β-air-cooled and **e** the 15%-rolled specimens; **b**, **d** and **f** IPF maps corresponding accordingly to **a**, **c** and **e**, with HABs and LABs indicated by black and gray lines, respectively. The color code for grain orientations in all these IPF maps is the same, as indicated in the inset in Fig. 2b. (Color figure online)

1.38–2.38 0>) between those α variants [26]. After referring to rotation axis distributions in Fig. 4b, one can know that the peak angles around 60° and 90° correspond to the second, third, fourth, and fifth Burgers misorientations [27]. With respect to the 15%-rolled specimen, Fig. 4c reveals that its MAD is distinctly different from that of the β-air cooled specimen. After the 15%-rolling, the prior peak near 60° is largely decayed while the prior peak near 90° is shifted towards lower angles to form a new peak around 85° with rotation axes focused on <11–20>. Such a new peak should be resulted from the formation of many {10–12} twins (Figs. 2 and 3). Besides, another misorientation angle peak near 3°–5° can be seen in Fig. 4c and its peak intensity is even higher than others. The presence of such a low-angle peak suggests that dense LABs are formed due to active dislocation slip. Note that specific slip modes activated in the 15%-rolled specimen can be probed by analyzing rotation axes corresponding to these low angles (more detailed illustration in Ref [28].). As shown in Fig. 4c, their rotation axes are concentrated on <0001>, suggesting prismatic <a> slip ({10–10} <11–20>) as the main slip mode [28]. In fact, the prismatic slip is also known to be the easiest slip system in α-Zr deformed at room temperature [29]. The above analysis demonstrates that both the prismatic slip and the {10–12} tensile twinning are readily initiated to accommodate the plastic strain during the 15% rolling.

Figure 5 presents EBSD kernel average misorientation (KAM) maps and distribution histograms. KAM values are known to be closely related to residual strains inside materials [30]. Figure 5a reveals that the KAM in the as-received specimen is relatively low and distributed uniformly. Its average KAM is calculated to be only 0.28° (Fig. 5b), indicating hardly any residual strains. For the β-air-cooled specimen, Fig. 5c shows that its KAM distribution is still relatively uniform while the average KAM is slightly increased to be 0.38° (Fig. 5d), compared to that of the as-received specimen. The increased KAM may be related to the phase-transformation stresses caused by

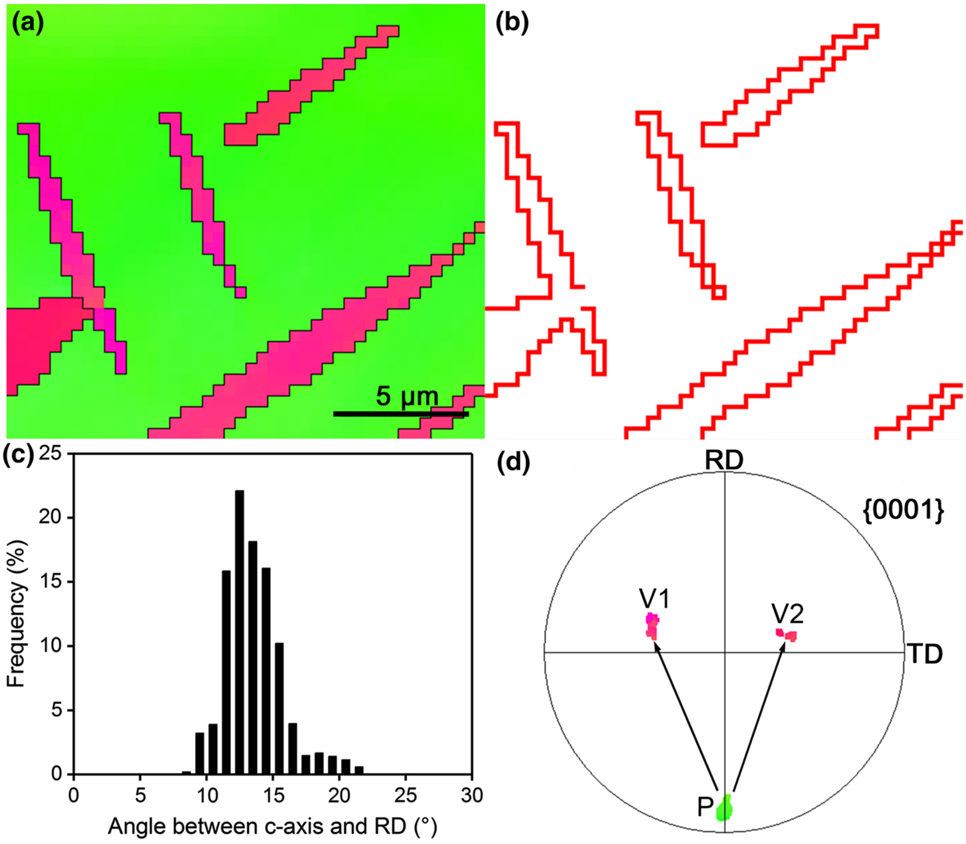

Fig. 3 Dedicated analyses on the boxed region in Fig. 2f: **a** IPF map, **b** grain boundary map, **c** angles between c-axis of the parent grain and the RD and **d** basal pole figure. The red lines in **b** represent boundaries with the misorientation of 85° ± 2°/<11–20>; "P" and "V" in **d** indicate the parent grain and twinning variants, respectively. (Color figure online)

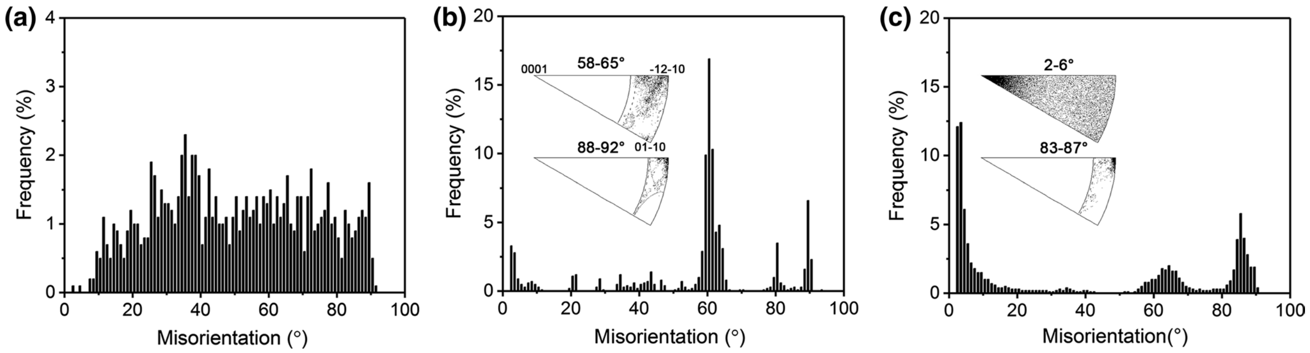

Fig. 4 Misorientation angle and rotation axis distributions of **a** the as-received, **b** the β-air-cooled and **c** the 15%-rolled specimens

structural discrepancies between β and α phases. Nevertheless, as the β-cooling rate in air is relatively low, residual strains are not allowed to be accumulated too much [31, 32]. Figure 5e and f show that after the 15% rolling, the KAM distribution becomes highly heterogeneous and the average value is markedly increased to be 0.76°. A comparison between Figs. 2f and 5e suggests that the KAM is higher near LABs and twin boundaries. This indicates that dislocation pile-ups are easier to occur in these places. From Fig. 5f, one can also seen that the KAM distribution of the 15%-rolled specimen is spread towards higher angles, suggesting the existence of strain gradients.

3.2 Hardness Analyses

Hardnesses of various specimens are measured and shown in Fig. 6. The average hardness of the as-received specimen is ~ 199 HV while it is decreased to ~ 170 HV after the β air cooling. For the 15%-rolled specimen, its hardness (~ 228 HV on average) is found to be higher than both the as-received and the β-air-cooled specimens. Reasons accounting for the hardness variation after the β air cooling and the subsequent rolling can be analyzed in light of the above microstructural characteristics. After the β air cooling, the average grain size is increased from 8.5 μm to

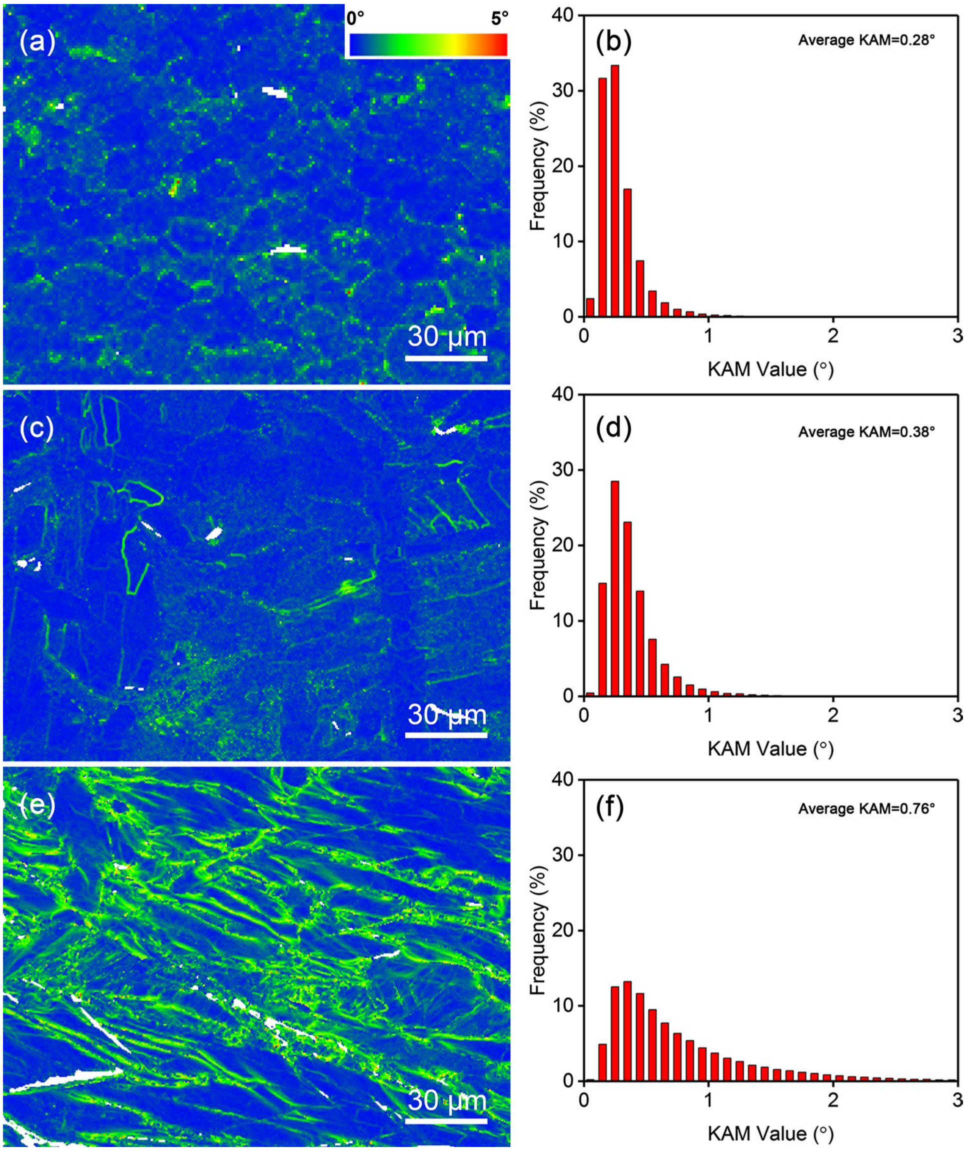

Fig. 5 KAM maps (only the three nearest neighbors considered) of **a** the as-received, **c** the β-air-cooled and **e** the 15%-rolled specimens; **b**, **d** and **f** KAM distribution histograms corresponding accordingly to **a**, **c** and **e**, respectively

14.5 μm. According to the Hall–Petch relation, the resistance of grain boundaries to dislocation movements would be weakened with increasing grain sizes [33]. This means that grain coarsening caused by the β air cooling should be an important factor for the hardness drop. Meanwhile, grain orientations of the β-air-cooled specimen are more scattered than those of the as-received specimen (Fig. 2b and d), allowing multiple deformation modes (both slip and twinning) to be initiated simultaneously [5]. This should have also led to the hardness decrease. Figure 1 shows that SPPs are presented in both the as-received and the β-air-cooled specimens and they may also have some contribution to hardness. Nevertheless, limited amounts of SPPs (< 0.5% in volume fraction) can be formed due to the low contents of alloying elements in Zr702, which could only bring minimal hardening effects [34].

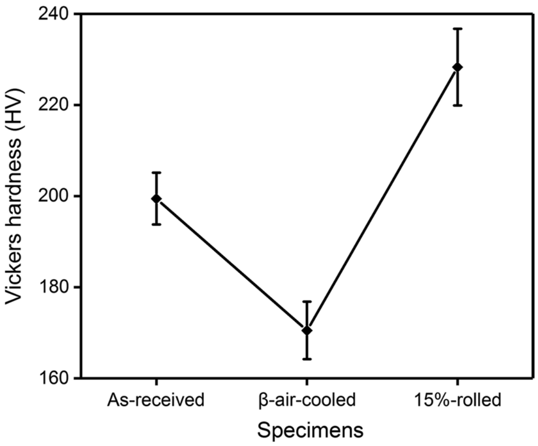

Fig. 6 Hardnesses of the as-received, the β-air-cooled and the 15%-rolled specimens

After the 15% rolling, the appearance of many twins reduces the average grain size to 5.7 μm (Fig. 2f) and the grain refinement must be responsible for the increased hardness. In addition, there are a large number of LABs in the 15%-rolled specimen (Figs. 2f and 4c), which are also able to effectively impede dislocation movements and contribute to hardening [35]. Such rolling-induced microstructural features are believed to lead to higher hardness for the 15%-rolled specimen, compared to both the as-received and β-air-cooled specimens.

4 Conclusions

1. After the β air cooling, the prior equiaxed grains in the as-received material are completely transformed into Widmanstätten structures featured by coarse plates, with average grain sizes increased from 8.5 to 14.5 μm. The subsequent 15% rolling readily activate both slip and twinning (especially the {10–12} type), leading to significant grain refinement (the average size 5.7 μm).
2. Typical phase transformation misorientations (two peaks around 60° and 90°) are produced in the β-air-cooled specimen, accompanied by scattered grain orientations. The active slip and twinning during the 15% rolling result in the appearance of new misorientation angle peaks around 3°–5° and 85°.
3. Hardness is decreased from ~ 199 HV to ~ 170 HV after the β air cooling, which can be ascribed to grain coarsening and the scattered orientations induced by the slow β → α transformation. Effective grain refinement by {10–12} twinning and denser LABs in the 15%-rolled specimen allow the hardness to be markedly increased to ~ 228 HV.

Acknowledgements This work was supported by the Fundamental and Cutting-Edge Research Plan of Chongqing (cstc2018jcyjAX0299 and cstc2017jcyjAX0114) and the National Natural Science Foundation of China (51601075).

References

1. Z. Duan, H. Yang, Y. Satoh, K. Murakami, S. Kano, Z. Zhao, J. Shen, H. Abe, Current status of materials development of nuclear fuel cladding tubes for light water reactors. Nucl. Eng. Des. **316**, 131–150 (2017)
2. S.J. Zinkle, G.S. Was, Materials challenges in nuclear energy. Acta Mater. **61**, 735–758 (2013)
3. C.C. Tang, M. Stueber, H.J. Seifert, M. Steinbrueck, Protective coatings on zirconium-based alloys as accident-tolerant fuel (ATF) claddings. Corros. Rev. **35**, 141–165 (2017)
4. K.L. Murty, I. Charit, Texture development and anisotropic deformation of zircaloys. Prog. Nucl. Energy. **48**, 325–359 (2006)
5. E. Tenckhoff, Review of deformation mechanisms, texture, and mechanical anisotropy in zirconium and zirconium base alloys. J. ASTM. Int. **2**, 25–50 (2005)
6. D. Fuloria, N. Kumar, R. Jayaganthan, S.K. Jha, D. Srivastava, An investigation of effect of annealing at different temperatures on microstructures and bulk textures development in deformed Zircaloy-4. Mater. Charact. **129**, 217–233 (2017)
7. J. Singh, S. Mahesh, G. Kumar, P. Pant, D. Srivastava, G. Dey, N. Saibaba, I. Samajdar, Texture development and plastic deformation in a pilgered Zircaloy-4 tube. Metall. Mater. Trans. A **46**, 1927–1947 (2015)
8. S. Goel, N. Keskar, R. Jayaganthan, I.V. Singh, D. Srivastava, G.K. Dey, N. Saibaba, Mechanical behaviour and microstructural characterizations of ultrafine grained Zircaloy-2 processed by cryorolling. Mater. Sci. Eng. A **603**, 23–29 (2014)
9. L. Chai, B. Luan, D. Xiao, M. Zhang, K.L. Murty, Q. Liu, Microstructural and textural evolution of commercially pure Zr sheet rolled at room and liquid nitrogen temperatures. Mater. Des. **85**, 296–308 (2015)
10. Z.N. Yang, Y.Y. Xiao, F.C. Zhang, Z.G. Yan, Effect of cold rolling on microstructure and mechanical properties of pure Zr. Mater. Sci. Eng. A **556**, 728–733 (2012)
11. A. Sarkar, K.L. Murty, Microstructure–mechanical property correlation of cryo rolled Zircaloy-4. J. Nucl. Mater. **456**, 287–291 (2015)
12. J. Romero, M. Preuss, J. Quinta da Fonseca, Texture memory and variant selection during phase transformation of a zirconium alloy. Acta Mater. **57**, 5501–5511 (2009)
13. H.G. Kim, J.H. Baek, S.D. Kim, Y.H. Jeong, Microstructure and corrosion characteristics of Zr–1.5Nb–0.4Sn–0.2Fe–0.1Cr alloy with a beta-annealing. J. Nucl. Mater. **372**, 304–311 (2008)
14. L. Chai, B. Luan, K.L. Murty, Q. Liu, Effect of predeformation on microstructural evolution of a Zr alloy during 550–700 °C aging after β quenching. Acta Mater. **61**, 3099–3109 (2013)
15. M.K. Kumar, C. Vanitha, I. Samajdar, G.K. Dey, R. Tewari, D. Srivastava, S. Banerjee, Deformation texture and microtexture developments in a cold rolled single phase hexagonal Zircaloy 2. Mater. Sci. Technol. **22**, 331–342 (2006)
16. S. Zaefferer, N.-N. Elhami, Theory and application of electron channelling contrast imaging under controlled diffraction conditions. Acta Mater. **75**, 20–50 (2014)
17. L. Chai, S. Wang, H. Wu, N. Guo, H. Pan, L. Chen, K.L. Murty, B. Song, α→β Transformation characteristics revealed by pulsed laser-induced non-equilibrium microstructures in duplex-phase Zr alloy. Sci. China Technol. Sci. **60**, 1255–1262 (2017)
18. L. Chai, B. Chen, S. Wang, N. Guo, C. Huang, Z. Zhou, W. Huang, Microstructural changes of Zr702 induced by pulsed laser surface treatment. Appl. Surf. Sci. **364**, 61–68 (2016)
19. A.R. Massih, V. Dahlback, M. Limback, T. Andersson, B. Lehtinen, Effect of beta-to-alpha phase transition rate on corrosion behaviour of zircaloy. Corros. Sci. **48**, 1154–1181 (2006)
20. L. Chai, B. Luan, J. Chen, J. Zhou, Q. Liu, Effect of cooling rate on β → α transformation during quenching of a Zr–0.85Sn–0.4Nb–0.4Fe–0.1Cr–0.05Cu alloy. Sci. China-Technol. Sci. **55**, 2960–2964 (2012)
21. L. Chai, B. Luan, B. Chen, H. Yang, Q. Liu, W. Huang, Concurrent inheritance of microstructure and texture after slow β→α cooling of commercially pure Zr. Sci. China Technol. Sci. **59**, 1771–1776 (2016)
22. S.K. Sahoo, V.D. Hiwarkar, I. Samajdar, G.K. Dey, D. Srivastav, R. Tiwari, S. Banerjee, Heterogeneous deformation in single-phase Zircaloy 2. Scripta Mater. **56**, 963–966 (2007)
23. R.D. Doherty, D.A. Hughes, F.J. Humphreys, J.J. Jonas, D.J. Jensen, M.E. Kassner, W.E. King, T.R. McNelley, H.J. McQueen, A.D. Rollett, Current issues in recrystallization: a review. Mater. Sci. Eng. A **238**, 219–274 (1997)

24. K.Y. Zhu, B. Bacroix, T. Chauveau, D. Chaubet, O. Castelnau, Texture evolution and associated nucleation and growth mechanisms during annealing of a Zr alloy. Metall. Mater. Trans. A **40**, 2423–2434 (2009)
25. W.G. Burgers, On the process of transition of the cubic-body-centered modification into the hexagonal-close-packed modification of zirconium. Physica. **1**, 561–586 (1934)
26. E. Farabi, P.D. Hodgson, G.S. Rohrer, H. Beladi, Five-parameter intervariant boundary characterization of martensite in commercially pure titanium. Acta Mater. **154**, 147–160 (2018)
27. L. Chai, B. Luan, M. Zhang, K.L. Murty, Q. Liu, Experimental observation of 12 α variants inherited from one β grain in a Zr alloy. J. Nucl. Mater. **440**, 377–381 (2013)
28. Y.B. Chun, M. Battaini, C.H.J. Davies, S.K. Hwang, Distribution characteristics of in-grain misorientation axes in cold-rolled commercially pure titanium and their correlation with active slip modes. Metall. Mater. Trans. A **41**, 3473–3487 (2010)
29. J. Gong, T.B. Britton, M.A. Cuddihy, F.P.E. Dunne, A.J. Wilkinson, <a> Prismatic, <a> basal, and <c + a> slip strengths of commercially pure Zr by micro-cantilever tests. Acta Mater. 96, 249–257 (2015).
30. S.I. Wright, M.M. Nowell, D.P. Field, A Review of strain analysis using electron backscatter diffraction. Microsc. Microanal. **17**, 316–329 (2011)
31. K.F. Ahmmed, M.R. Daymond, M.A. Gharghouri, Microstructural evaluation and crystallographic texture modification of heat-treated zirconium Excel pressure tube material. J. Alloy Compd. **687**, 1021–1033 (2016)
32. C.N. Tomé, N. Christodoulou, P.A. Turner, M.A. Miller, C.H. Woo, J. Root, T.M. Holden, Role of internal stresses in the transient of irradiation growth of Zircaloy-2. J. Nucl. Mater. **227**, 237–250 (1996)
33. R.W. Armstrong, Hall–Petch description of nanopolycrystalline Cu, Ni and Al strength levels and strain rate sensitivities. Philos. Mag. **96**, 3097–3108 (2016)
34. P. Gopalan, R. Rajaraman, G. Amarendra, C.S. Sundar, B. Viswanathan, T. Jayakumar, P. Palanichamy, B. Raj, Characterisation of β-quenched and thermally aged Zircaloy-2 by positron annihilation, hardness and ultrasonic velocity measurements. J. Nucl. Mater. **345**, 162–166 (2005)
35. N. Hansen, Hall–Petch relation and boundary strengthening. Scripta Mater. **51**, 801–806 (2004)